JAAS

ROYAL SOCIETY OF CHEMISTRY

PAPER

View Article Online
View Journal | View Issue

Check for updates

Cite this: *J. Anal. At. Spectrom.*, 2025, **40**, 2753

In situ micro-beam U–Pb dating of apatite using CAMECA 1300HR^3 LG-SIMS

Yue Guan,[a] Jun-Yong Li,[a] Allen K. Kennedy,[b] De-Hong Du,[a] Lan-Lan Tian,[a] Wen-Li Xie[a] and Xiao-Lei Wang *[a]

Apatite is a U-bearing mineral commonly present in planetary materials and has been widely used for geochronological studies. However, precise *in situ* U–Pb dating of tiny apatite (grain size <15 μm) remains challenging due to its low abundance of uranium (U) and radiogenic lead (Pb). To address this issue, we have developed two micro-beam analytical methods (*i.e.*, 5 nA and 500 pA primary beams) using three apatite reference materials (BR5, AFG2, and Otter lake) and a CAMECA IMS 1300HR^3 large-geometry secondary ion mass spectrometry (LG-SIMS). The 5 nA method (mono) produces a larger sputter crater (12.5 × 12.5 × 4.1 μm) and achieves higher dating precision, with age errors (n = 20) of <0.5% (1σ) for BR5, <2.5% (1σ) for AFG2, and <0.7% (1σ) for Otter lake. In contrast, the 500 pA method (multi) produces a smaller sputter crater (5.3 × 5.3 × 1.4 μm) that results in lower dating precision, with age errors (n = 25) of <1.3% (1σ) for BR5, <4.1% (1σ) for AFG2, and <1.8% (1σ) for Otter lake. Both methods yield accurate ages within the uncertainties and are applicable for apatite U–Pb dating. For data reduction, we recommend the use of the Pb/U *vs.* UO_2/U calibration protocol, because it introduces less age bias compared to those of Pb/U *vs.* UO/U and Pb/UO *vs.* UO_2/UO protocols. The methodological approaches of this study enable high-precision *in situ* U–Pb dating of tiny apatite and they will expand the application of LG-SIMS in geochronological studies of (extra-) terrestrial apatite samples.

Received 8th July 2025
Accepted 11th August 2025

DOI: 10.1039/d5ja00266d

rsc.li/jaas

Published on 15 August 2025. Downloaded by NANJING UNIVERSITY on 1/21/2026 8:15:39 AM.

1. Introduction

Apatite [$Ca_5(PO_4)_3$(F, Cl, OH)] is a ubiquitous mineral phase in igneous, sedimentary, and metamorphic rocks that typically incorporates high concentrations of U, Pb, Th, REEs, Sr, and other trace elements. Its U–Pb systematics are regarded as a powerful "age probe" that has been widely used in both geochronological and thermochronological studies.[1–4] Integrating apatite ages with other geochemical data (*e.g.*, REE, F, Cl, S) can provide critical insights into a range of mid- to high-temperature geological processes, including fluid–rock interaction and metasomatism,[5] metamorphism[6–9] and magmatic differentiation.[10]

Secondary ion mass spectrometry (SIMS) *in situ* analysis features high precision, high spatial resolution, and minimal sample consumption and has been widely applied to apatite U–Pb dating.[6,8,9,11,12] The occurrence of abundant tiny apatite in breccia and basalt clasts returned by the recent Chang'e-5 and Chang'e-6 lunar missions,[12–18] makes micro-dating of apatite a high priority. However, lower U concentration and higher common Pb to radiogenic Pb ratios compared to zircon,[19] as well as generally lower Pb yields,[20–22] make achieving precise U–Pb ages of tiny apatite with sizes smaller than 15 μm very challenging. Obtaining high-precision dates for these grains is crucial for reconstructing lunar magmatic and impact histories.[23–25]

In this study, we develop two *in situ* SIMS U–Pb analytical methods targeted at dating tiny apatite (<15 μm). The two methods were compared in terms of ablation depth, analytical precision, and correction parameters. Furthermore, we evaluated the feasibility and value of three U–Pb calibration protocols during data reduction of apatite LG-SIMS U–Pb data.

2. Analytical methods

2.1 Sample preparation

We employed three gem-grade apatite reference materials (BR5, AFG2, and Otter lake) with well-constrained crystallization ages for U–Pb dating analysis. Kennedy *et al.*[26] determined the crystallization ages of BR5 and AFG2: BR5 yields an ID-TIMS U–Pb concordia age of 2040.34 ± 0.18 Ma (n = 7, 2σ) and a Sensitive High Resolution Ion Micro Probe (SHRIMP) U–Pb concordia age of 2044.7 ± 6.3 Ma (n = 126, 2σ); AFG2 displays a SHRIMP U–Pb concordia age of 477.1 ± 1.5 Ma (n = 140, 2σ) and an ID-TIMS U–Pb concordia age of 478.71 ± 0.22 Ma (n = 10, 2σ). Notably, BR5 contains low and homogeneous common Pb,[26] rendering it particularly suitable for U–Pb calibration. Chew *et al.*[27] reported the Otter lake apatite's crystallization age with a Lu-Hf isochron

[a]*State Key Laboratory of Critical Earth Material Cycling and Mineral Deposits, School of Earth Sciences and Engineering, Nanjing University, Nanjing 210023, China. E-mail: wxl@nju.edu.cn*

[b]*John de Later Centre, Curtin University, Kent. St., Bentley, 6102, Western Australia*

Published on 15 August 2025. Downloaded by NANJING UNIVERSITY on 1/21/2026 8:15:39 AM.

age of 998 ± 6 Ma ($\lambda^{176}Lu = 1.93 \times 10^{-11}$/year, MSWD = 1.7, 2σ). In this study, we adopt the ID-TIMS age of 2040.34 ± 0.18 Ma for the BR5, the ID-TIMS age of 478.71 ± 0.22 Ma for the AFG2, and Lu-Hf age of 998 ± 6 Ma for the Otter lake (N. B. this apatite is different to the Otter Lake apatites of Kennedy *et al.*[26]).

We mounted the BR5, AFG2, and Otter lake apatite grains in an epoxy resin matrix. They were initially polished with a 3-μm diamond suspension, followed by a further polishing step using a 1-μm diamond suspension. Subsequently, the samples received a meticulous polish with 0.5-μm silicon oxide particles. After thorough cleaning with deionized water and anhydrous ethanol, they were coated with a ~20 nm gold layer.

2.2 SIMS analytical procedures

We designed two analytical methods for tiny apatite U–Pb dating using the IMS 1300HR^3 LG-SIMS at the State Key Laboratory of Critical Earth Material Cycling and Mineral Deposits, Nanjing University. Table 1 gives details of ion optical parameters.

The first method employed a 5 nA shaped primary beam ($^{16}O_2^-$, Köhler mode) to analyze the three apatite reference materials. Positive secondary ions were accelerated with a 10 kV potential. To resolve isobaric interferences, we collected the secondary ions by a central off-axis Mono-Electronic Multiplier (EM) at a Mass Resolution Power (MRP) of 6000 with a 70 μm entrance slit and a 50 eV energy window. Prior to each analysis, we applied a 70-second pre-sputter using a 20 × 20 μm raster to remove the gold coating and clean the surface. Then, a 5 × 5 μm raster was used to reduce any crater depth related effect on secondary ion yields during the analysis. This method measured the ion species of $^{204}Pb^+$, $^{206}Pb^+$, $^{207}Pb^+$, $^{208}Pb^+$, $^{232}Th^+$, $^{238}U^+$, $^{232}Th^{16}O^+$, $^{238}U^{16}O^+$ and $^{238}U^{16}O_2^+$, using a peak jumping mode. The total duration for one single analysis was ~11 minutes with 7 cycles. We used the $^{230}Th^{16}O^+$ ion as the centering peak for mass centering.

The second method employed a 500 pA $^{16}O^-$ Gaussian primary beam, which was focused to a diameter of ~3 μm with a −13 kV acceleration potential. This method had the same settings of max area, contrast aperture, entrance slit, field aperture and the energy slit as the first method. We used four multi-collector electron multipliers (Multi-EMs) with a MPR of 5000 to collect the secondary ions. This method detected the ion species $^{204}Pb^+$, $^{206}Pb^+$, $^{207}Pb^+$, $^{208}Pb^+$, $^{238}U^+$, $^{238}U^{16}O^+$, $^{238}U^{16}O_2^+$, $^{232}Th^+$ and $^{232}Th^{16}O^+$ by the Multi-EMs (L2, L1, C and H2). The three Pb isotope secondary ion species $^{204}Pb^+$, $^{206}Pb^+$ and $^{207}Pb^+$ were detected on the Multi-EMs (L2, L1 and C) with a 60 s counting time, while collected other ion species on the H2 EM, except for $^{238}U^+$ on L1. The details of the analysis sequence are listed in Appendix 1 (SI). We corrected the relative yields of Multi-EMs using Pb isotopes from the BCR glass prior of all analyses. The long-term noise of EMs was less than 0.002 c/s. Prior to data collection, we used an 80 s pre-sputter 20 × 20 μm raster with the 5 nA $^{16}O^-$ primary beam to clean the sample surface. During measurement, raster was switched off. The total analytical time for each spot was ~23 minutes with 10 cycles.

Table 1 Parameter settings of the two analytical methods using SIMS

	Method 1	Method 2
Primary beam	5 nA O_2^- shaped beam	500 pA O^- Gaussian beam
Collection mode	Mono	Multi
Centering peak	$^{232}Th\ ^{16}O^+$	$^{232}Th\ ^{16}O^+$
MRP	6000 in mono	5000 in multi;
Field aperture (μm)	5000	
Entrance slit (μm)	70	
Energy slit (μm)	50	
Contrast aperture (μm)	400	
Max area	40	
Raster size (μm)	5	0
Pre-sputtering time raster	70 s, 20 μm (5 nA)	80 s, 20 μm (5 nA)
Analysis time	11 min	23 min
Analysis sequence	See appendix 1 (SI)	

2.3 Characterization of beam sputter craters

After U–Pb dating analyses, we re-coated the sample surfaces with a thin gold film to enhance electrical conductivity and optimize secondary electron emission for scanning electron microscopy (SEM) imaging. We used a Thermo Fisher Phenom XL SEM with the lateral resolution of ~8 nm to examine the sputter crater morphologies. We collected the SEM images at an accelerating voltage of 10 kV under a chamber pressure of 0.1 Pa. Then, we used a CHOST (Suzhou) Super-View W1 white light interferometric profiler with a vertical resolution of 2 nm to perform three-dimensional (3D) topographic measurements to precisely quantify crater depths. This dual-method approach allowed much better characterization of the 3D morphologies of beam sputter craters at both micro- and nano-scales.

3. Data reducing protocol

3.1 Pb/U calibration

There is significant inter-elemental fractionation between Pb and U during SIMS analysis, which is commonly attributed to their different ionization behaviors,[19,28] *i.e.*, Pb ionizes exclusively as Pb^+, whereas U can form multiple ionic species of U^+, UO^+, and UO_2^+ during sputtering. In addition to that, the ionization efficiencies of Pb and U may differ, further contributing to the observed fractionation[19] (unless otherwise specified, Pb and U refer to ^{206}Pb and ^{238}U respectively in this work). Therefore, in order to achieve the real Pb/U ratio, the calibration of inter-elemental fractionation is necessary. The $^{206}Pb^+/^{238}U^+$ *vs.* $^{238}U^{16}O^+/^{238}U^+$, $^{206}Pb^+/^{238}U^+$ *vs.* $^{238}U^{16}O_2^+/^{238}U^+$ and $^{206}Pb^+/^{238}U^{16}O^+$ *vs.* $^{238}U^{16}O_2^+/^{238}U^{16}O^+$ were simplified as Pb/U *vs.* UO/U, Pb/U *vs.* UO_2/U and Pb/UO *vs.* UO_2/UO in the rest of the paper.

The basic underlying assumption used in SIMS U–Pb data reduction is incorporated in the following equation:

$$\frac{\frac{^{206}Pb}{^{238}U_{un}}}{\frac{^{206}Pb}{^{238}U_{st}}} = \frac{\frac{^{206}Pb^+}{^{238}U_{un}^+}}{\frac{^{206}Pb^+}{^{238}U_{st}^+}} \quad (1)$$

 This journal is © The Royal Society of Chemistry 2025

Published on 15 August 2025. Downloaded by NANJING UNIVERSITY on 1/21/2026 8:15:39 AM.

where the $^{206}Pb^{+}$ represents the ionized form of the radiogenic ^{206}Pb isotope. Typically, the measured $^{206}Pb^{+}/^{238}U^{+}$ ratio exceeds the actual $^{206}Pb/^{238}U$ ratio due to variations in the ionization behavior. Consequently, the utilization of a matrix-matched reference material is essential for SIMS U–Pb analyses. Under identical matrix and instrumental conditions, both the sample and the reference material exhibit a consistent correlation between $^{206}Pb^{+}/^{238}U^{+}$ and $^{238}U^{16}O_x^{+}/^{238}U^{+}$ ratios ($x = 1$ or 2, throughout the text). This relationship may follow a linear, quadratic or power law. Previous studies have used different correlations between $^{206}Pb^{+}/^{238}U^{+}$ and $^{238}U^{16}O_x^{+}/^{238}U^{16}O_y^{+}$ ($x = 1, 2; y = 0, 1; x \neq y$.) for different minerals.[29–32] The power law relationships have been demonstrated to be more suitable for LG-SIMS.[28,33]

The common apatite U–Pb calibration protocol can be described by:

$$\ln\left(^{206}Pb^{+}/^{238}U^{+}\right) = a\ln\left(^{238}U^{16}O_{x=1,2}{}^{+}/^{238}U^{+}\right) + b \quad (2)$$

where a and b are the constants. The values of the two constants can be determined using the reference material data which are shown on the plots (Fig. 1). Then, the eqn (1) can be rewritten as:

$$\frac{\left(^{206}Pb/^{238}U\right)_{un}}{\left(^{206}Pb/^{238}U\right)_{st}} = \frac{\left(^{206}Pb^{+}/^{238}U^{+}\right)_{un}}{e^{a\ln\left(^{238}U^{16}O_x{}^{+}/^{238}U^{+}\right)_{st}+b}} = \frac{\left(^{206}Pb^{+}/^{238}U^{+}\right)_{un}}{e^{a\ln\left(^{238}U^{16}O_x{}^{+}/^{238}U^{+}\right)_{st}}}, \quad (3)$$

Based on the Local Thermodynamic Equilibrium (LTE) model,[34] sputtering process underlying the production of the $^{238}U^{16}O_x^{+}/^{238}U^{+}$ ratio is analogous if the matrix is identical. Consequently, the term $(^{238}U^{16}O_x^{+}/^{238}U^{+})_{st}$ in eqn (3) can be replaced by $(^{238}U^{16}O_x^{+}/^{238}U^{+})_{un}$. Thereby, the unfractionated ratio $(^{206}Pb^{+}/^{238}U^{+})_{un}$ can be derived from the eqn (3) as:

$$\left(^{206}Pb/^{238}U\right)_{un} = \frac{\left(^{206}Pb/^{238}U\right)_{st}\left(^{206}Pb^{+}/^{238}U^{+}\right)_{un}}{e^{b\left(^{238}U^{16}O_x{}^{+}/^{238}U^{+}\right)_{un}}}, \quad (4)$$

where the constants a, b are derived by linear regression of the measured ratios $\ln(^{206}Pb^{+}/^{238}U^{+})_{st}$ and $\ln(^{238}U^{16}O_x^{+}/^{238}U^{+})_{st}$. Here, $(^{206}Pb/^{238}U)_{st}$ represents a constant value, while $(^{206}Pb^{+}/^{238}U^{+})_{un}$ and $(^{238}U^{16}O_x^{+}/^{238}U^{+})_{un}$ are measured values. The uncertainty in the ratio $(^{206}Pb/^{238}U)_{un}$ is primarily influenced by the internal error of $(^{206}Pb^{+}/^{238}U^{+})_{un}$ and the uncertainty of the coefficient a. Therefore, a precisely fitted power law

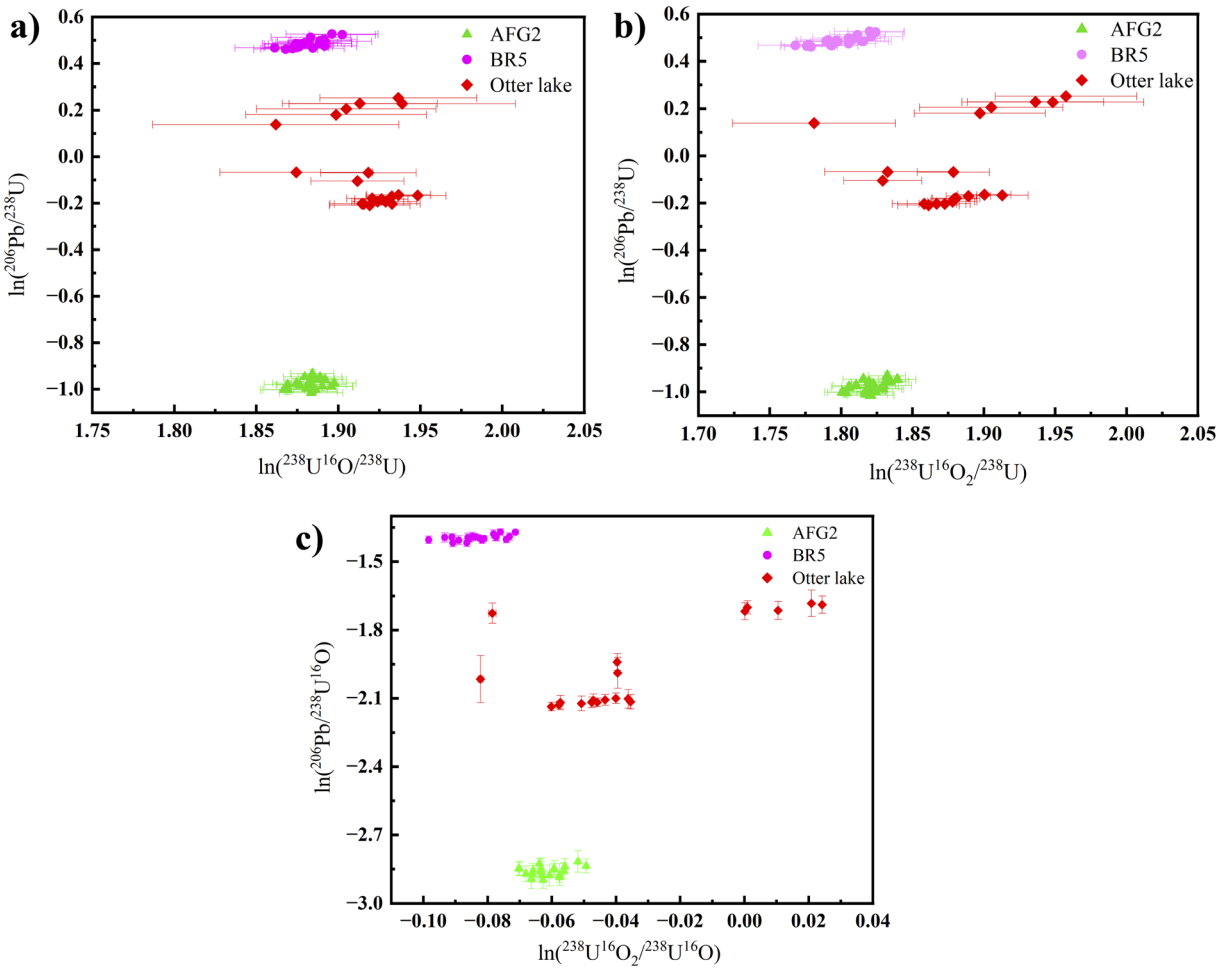

Fig. 1 Calibration diagrams for the three apatite reference materials using a 5 nA method. (a) $\ln(^{206}Pb^{+}/^{238}U^{+})$ *vs.* $\ln(^{238}U^{16}O^{+}/^{238}U^{+})$ plot; (b) $\ln(^{206}Pb^{+}/^{238}U^{+})$ *vs.* $\ln(^{238}U^{16}O_2{}^{+}/^{238}U^{+})$ plot; (c) $\ln(^{206}Pb^{+}/^{238}U^{16}O^{+})$ *vs.* $\ln(^{238}U^{16}O_2{}^{+}/^{238}U^{16}O^{+})$ plot.

Published on 15 August 2025. Downloaded by NANJING UNIVERSITY on 1/21/2026 8:15:39 AM.

for the reference material is essential for achieving accurate U–Pb age. For SHRIMP U–Pb dating, the correlation between $^{206}Pb^{+}/^{238}U^{+}$ and $^{238}U^{16}O^{+}/^{238}U^{+}$, as well as $^{206}Pb^{+}/^{238}U^{16}O^{+}$ and $^{238}U^{16}O^{+}/^{238}U^{+}$, is commonly applied.[28] In the case of CAMECA SIMS, the correlation between $^{206}Pb^{+}/^{238}U^{+}$ and $^{238}U^{16}O_2{}^{+}/^{238}U^{+}$ appears to be better.[33]

In this study, we used the three power relationships (Pb/U *vs.* UO/U, Pb/U *vs.* UO_2/U, Pb/UO *vs.* UO_2/UO) to calibrate the U–Pb elemental fractionation of the apatite reference materials. We selected BR5 to calibrate all reference apatites owing to its low and relatively homogeneous common Pb concentration that permits more accurate U–Pb age determinations.[26] In this study, we applied U–Pb fractionation calibration without common Pb correction for BR5 because its common Pb is low and homogeneous, exerting almost no effect on the calibration fit lines. All ages were calculated using the decay constants recommended by Steiger and Jäger,[35] and the calculation routines of software *Isoplot 4.15.*[36] The resulting regression and weighted average ages are quoted at the 2σ error interval.

3.2 Common Pb calibration

The correction for common Pb is essential for determining accurate ages of apatite, since the initial Pb can account for a large proportion of the total Pb (typically, $^{206}Pb_{initial}/^{206}Pb_{total}$ vary from 0.01 to 0.5).[19,28] There are three usual methods for common Pb correction during data reducing. Firstly, based on the counts of ^{204}Pb, the proportion of $^{206}Pb^{*}/^{206}Pb_{total}$ (*represents radiogenic) can be used to correct the ratio of $^{206}Pb/^{238}U$ and $^{207}Pb/^{206}Pb$. This correction method has been well used in zircon data reducing. However, for apatite, the initial ^{204}Pb may have a more significant impact on these ratios than in zircon. Another approach is ^{207}Pb-based common Pb calibration, where an estimated ratio of $^{207}Pb^{*}/^{206}Pb^{*}$ is used to reduce the $^{206}Pb/^{238}U$ ratio. This approach is equivalent in effectiveness to plotting the Tera-Wasserburg Concordia with uncorrected data.[19] The high Th/U of apatite here precludes the common Pb correction method using ^{208}Pb.[26] The third method involves a 3-dimensional linear regression (Total Pb/U Isochron), necessitating that a line in $^{238}U/^{206}Pb$ – $^{204}Pb/^{206}Pb$ – $^{207}Pb/^{206}Pb$ space can be defined in cogenetic samples possess the same Pb isotopic compositions with an undisturbed U–Pb system.[37] This line has two intersections with two coordinate planes. The intersection with the $^{238}U/^{206}Pb$ – $^{207}Pb/^{206}Pb$ plane defines the age, while the intersection with the $^{207}Pb/^{206}Pb$ – $^{204}Pb/^{206}Pb$ plane determines the initial Pb isotopic composition. In this study, we adopted the third approach (given above) to derive U–Pb concordia ages for all U–Pb data from both methods. This approach combined the measured ratio of $^{204}Pb/^{206}Pb$ and $^{207}Pb/^{206}Pb$ for calculating the initial Pb isotopic composition to constrain the concordia age. For terrestrial samples, the initial common Pb can be applied to constrain the age for a better estimate.[28] Regarding to the extraterrestrial samples, this calibration method can help to derive the initial Pb composition and yields possibly the smallest error for the U/Pb or Pb/Pb isochron as all relevant isotope ratios are used at the same time.[27,38]

3.3 Pb/Th calibration

As with the Pb/U calibration, a linear relationship also exists between $\ln(^{208}Pb^{*+}/Th^{+})$ and $\ln(ThO^{+}/Th^{+})$ in SIMS analysis. Therefore, an analogous calibration approach was applied on the correction of Pb/Th fractionation. BR5 apatite was also used for deriving the correction factors of the power law relationship with $^{208}Pb^{*+}/Th^{+} = A \times (ThO^{+}/Th^{+})^{B}$. Both methods can acquire the Pb/Th ages. In respect of the structure of this study, the results are presented in Appendix 2 (SI).

3.4 Calibration of U and Th concentrations

In this study, we calculated Th and U concentrations directly from the raw counts of $^{230}Th^{16}O^{+}$ and $^{238}U^{16}O^{+}$ ions compared to those of the reference value without normalization as shown in eqn (5). We selected the AFG2 apatite as the reference material to calibrate the concentrations of other two apatite standards, due to its homogeneous Th and U concentrations.[26]

$$Th_{un} = \frac{\left(^{230}Th^{16}O^{+}\right)_{un}}{\left(^{230}Th^{16}O^{+}\right)_{st}} Th_{st} \quad (5)$$

4. Results

4.1 Topography of sputter craters

Fig. 2a and c show the ablation crater morphologies generated by the two primary beams currents. The two methods produce smaller craters of 5.3 × 5.3 × 1.4 μm (500 pA O^{-} beam) and 12.5 × 12.5 × 4.1 μm (5 nA $O_2{}^{-}$ shaped beam) compared to those of previous *in situ* apatite U–Pb dating methods (>15 μm spot sizes),[9,19,26,39] indicating a significant improvement in spatial resolution. Here the smaller craters result from the Oregon Physics Hyperion II Dual Polarity radio frequency (RF) ion source which has approximately twice the beam intensity of a conventional Duo ion source.[40] Based on the established apatite density of 3.18 g cm^{-3},[41] these craters correspond to exceptionally low sample consumption rates of ~0.533 ng and 0.03 ng per analysis, respectively. Therefore, apatite inclusions or apatite grains in lunar return samples, which typically range from 5 to 20 μm in size,[11,15,16] can be effectively analyzed for *in situ* SIMS U–Pb ages using the two methods described here.

4.2 U–Pb dating results of a 5 nA-beam method

We conducted 20 analyses for each apatite reference material, BR5, AFG2, and Otter lake. Method verification was achieved by establishing a linear regression between $^{207}Pb/^{206}Pb$ and $^{204}Pb/^{206}Pb$ ratios for BR5 apatite (Fig. 3), yielding a $^{207}Pb^{*}/^{206}Pb^{*}$ isochron age of 2042 ± 33 Ma (MSWD = 1.3) that is consistent with the published reference values.[26] The results from both methods were plotted on 3-D concordia diagrams using three isotopic ratios $^{238}U/^{206}Pb$, $^{207}Pb/^{206}Pb$ and $^{204}Pb/^{206}Pb$ along with their errors. Except the BR5 results in Fig. 4a1–3 anchored the upper intercept at initial Pb isotopic composition derived by Stacey and Kramers,[45] the other results have no anchored point in the $^{207}Pb/^{206}Pb$ – $^{204}Pb/^{206}Pb$ plane.

 This journal is © The Royal Society of Chemistry 2025

Published on 15 August 2025. Downloaded by NANJING UNIVERSITY on 1/21/2026 8:15:39 AM.

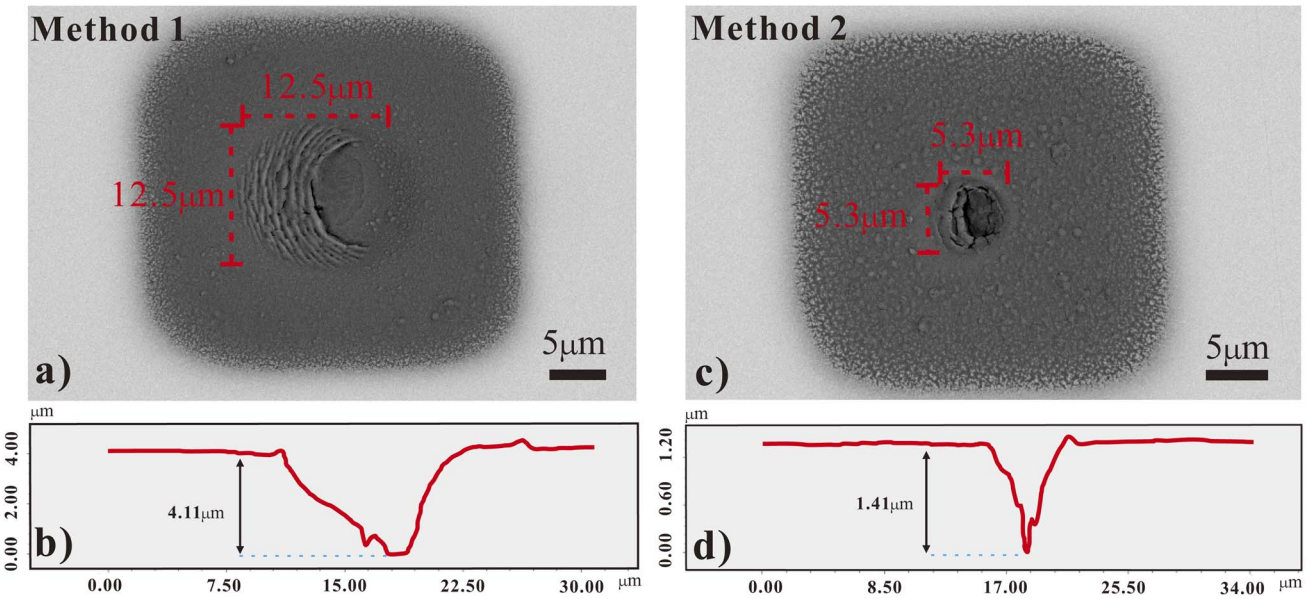

Fig. 2 Topography of sputter craters. (a) The secondary electron image of 5 nA $^{16}O_2^-$ beam crater on apatite; (b) the 3D white light profiler results of the 5 nA $^{16}O_2^-$ beam crater; (c) the secondary electron image of 500 pA $^{16}O^-$ beam crater on apatite; (d) the 3D white light profiler results of the 500 pA $^{16}O^-$ beam crater.

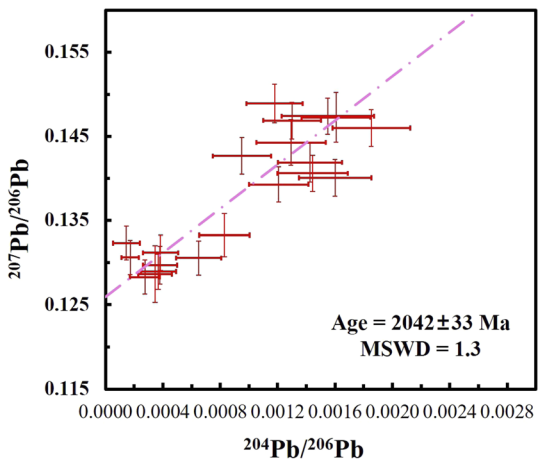

Fig. 3 The $^{207}Pb^*/^{206}Pb^*$ isochron age of BR5 apatite analyzed by 5 nA primary beam (data-point error crosses are 2σ).

The data points in 3-D space (red cross in Fig. 4 and 5) were constrained on the $^{238}U/^{206}Pb$ – $^{207}Pb/^{206}Pb$ plane (green cross in Fig. 4 and 5). The 3-D concordia plots for BR5 (Fig. 4) demonstrate three statistically robust intercept ages: 2035 ± 18 Ma (2σ, MSWD = 0.62), 2038 ± 18 Ma (2σ, MSWD = 0.51) and 2037 ± 16 Ma (2σ, MSWD = 0.69), which respectively correspond to the three different fractionation correction protocols[29] (Pb/U *vs.* UO/U, Pb/U *vs.* UO_2/U, and Pb/UO *vs.* UO_2/UO, respectively). Since BR5 serves as the reference material in this study, the accuracy of its U–Pb age cannot be properly assessed by either method. The $^{238}U/^{206}Pb$–$^{207}Pb/^{206}Pb$–$^{204}Pb/^{206}Pb$ 3-D concordia diagrams for AFG2 give three intercept ages: 481 ± 24 Ma (2σ, MSWD = 0.76), 480 ± 24 Ma (2σ, MSWD = 0.72) and 473 ± 23 Ma (2σ, MSWD = 0.73). The green cross points with error bounds represent the constrained intersections of the data points with the $^{238}U/^{206}Pb$–$^{207}Pb/^{206}Pb$ plane. The three U–Pb ages for AFG2 apatite are consistent with the reported ID-TIMS reference age of 478.71 ± 0.22 Ma (ref. 26) within analytical uncertainties. For the Otter Lake apatite, the different fractionation correction protocols[29] produce three identical ages, within uncertainties. They are: 990 ± 14 Ma (2σ, MSWD = 1.18), 991 ± 14 Ma (2σ, MSWD = 1.18) and 988 ± 12 Ma (2σ, MSWD = 1.3), excluding one abnormal spot Otterlake@5.

BR5 has homogeneous U and Th concentrations of 60 ± 3 ppm (1SD) and 869 ± 72 ppm (1SD), respectively, yielding a consistent Th/U ratio of 14.6 ± 1.2 (1SD, n = 20). Similarly, AFG2 apatite grains have uniform U (132 ± 4 ppm, 1SD) and Th (2051 ± 35 ppm, 1SD) concentrations, resulting in a well-constrained Th/U ratio of 15.5 ± 0.23 (1SD). As AFG2 served as the calibration standard for U and Th concentrations, its accuracy was not evaluated. However, Otter lake apatite has variable U and Th concentrations, with ranges of 9 to 96 ppm and 33 ppm to 758 ppm respectively, and Th/U ratios from 3.7 to 40.4. More details are given in Appendix 2 (SI).

4.3 U–Pb dating results of a 500 pA-beam method

Twenty-five analytical measurements were performed on each apatite reference material with a 500 pA micro-primary beam. The three-dimensional constrained Concordia data and ages are shown in Fig. 5. For the BR5 apatite, the Pb/U *vs.* UO/U and Pb/U *vs.* UO_2/U calibration procedure yielded intercept ages of 2039 ± 52 Ma (2σ, MSWD = 0.63) and 2040 ± 55 Ma (2σ, MSWD = 0.51), respectively. However, the Pb/UO *vs.* UO_2/UO calibration produced a significantly deviated intercept age of 1876 ± 89 Ma (2σ, MSWD = 1.03), which is inconsistent with the established reference age. The AFG2 apatite yields three different

Published on 15 August 2025. Downloaded by NANJING UNIVERSITY on 1/21/2026 8:15:39 AM.

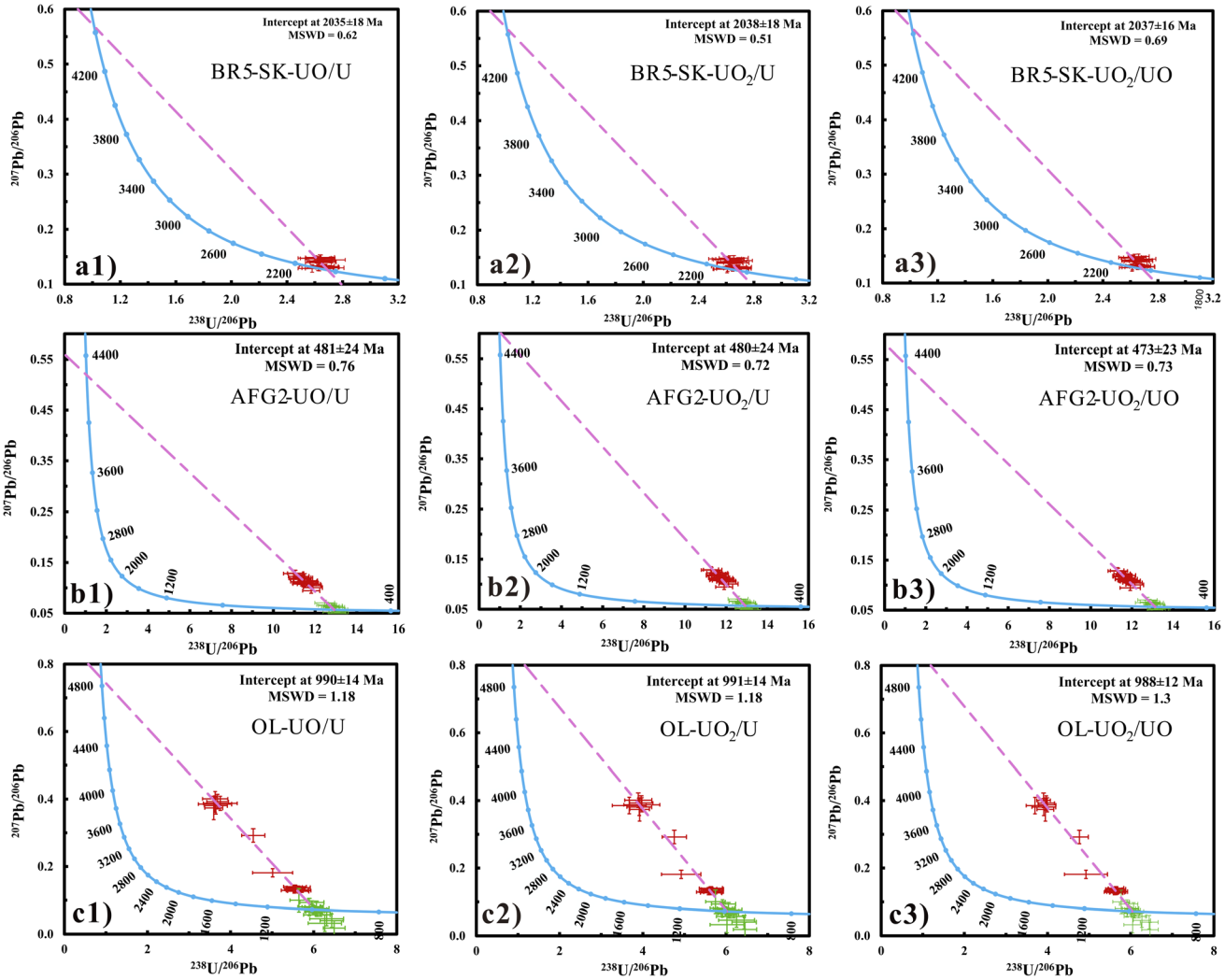

Fig. 4 The 3-D constrained concordia ages of BR5 (a1–a3) AFG2 (b1–b3) and Otter lake (c1–c3) apatites analyzed by the 5 nA ($^{16}O_2^-$) primary beam (n = 20 except Otter lake n = 19, data-point error crosses are 2σ for all results).

ages of 492 ± 38 Ma (2σ, MSWD = 0.68), 486 ± 40 Ma (2σ, MSWD = 0.7), and 449 ± 23 Ma (2σ, MSWD = 0.62) when using the three distinct calibration procedures. Similarly, the Otter lake apatite yields three intercept ages of 997 ± 36 Ma (2σ, MSWD = 1.9), 977 ± 36 Ma (2σ, MSWD = 2.0), and 899 ± 34 Ma (2σ, MSWD = 2.0), respectively. Additional geochemical data including Th, U, and Pb concentrations for the second method are provided in Appendix 2 (SI).

5. Discussion

The accuracy and precision of *in situ* SIMS U–Pb dating are primarily governed by two key factors: (1) the analytical Pb*/U ratio ($^{206}Pb^+/^{238}U^+$ after inter-elemental and common Pb correction), and (2) the adopted calibration protocols. We used the AFG2 U–Pb results to evaluate the two micro-beam methods and the three calibration protocols. The results of AFG2 are summarized in Table 2 and can be used for comparison of methods and protocols. The Pb*/U error represents a combined uncertainty of the measured relative standard error (RSE) of the raw ratios ($^{206}Pb^+/^{238}U^+$, $^{206}Pb^+/^{238}UO^+$) and the uncertainty associated with the power law relationships (Pb/U *vs.* UO_2 (UO)/U, Pb/UO *vs.* UO_2/UO) derived from the BR5 apatite standard. The error and bias of the intercept ages were obtained from the concordia age error and the deviation from the recommend values.

5.1 Comparison of Pb/U errors for two analytical methods

The secondary ion yields of $^{238}U^+$ and $^{206}Pb^+$ ions in apatite, which dominate the error of the Pb*/U ratio, are 1.3 and 1.6 cps $ppm^{-1}nA^{-1}$ for a 5 nA O_2^- primary beam, and 0.45 and 0.65 cps $ppm^{-1}nA^{-1}$ for a 500 pA O^- primary beam. As shown in Table 2, it is obvious that low yields for $^{238}U^+$ and $^{206}Pb^+$ lead to a larger the U–Pb error for the same apatite reference material (with homogeneous U and Pb content). In addition to ion yields, depth effects can also increase the error of the ratios because the V-shaped Gaussian primary beam could introduce additional uncertainty in the ratios over N cycles if no raster is applied.[42]

 This journal is © The Royal Society of Chemistry 2025

Published on 15 August 2025. Downloaded by NANJING UNIVERSITY on 1/21/2026 8:15:39 AM.

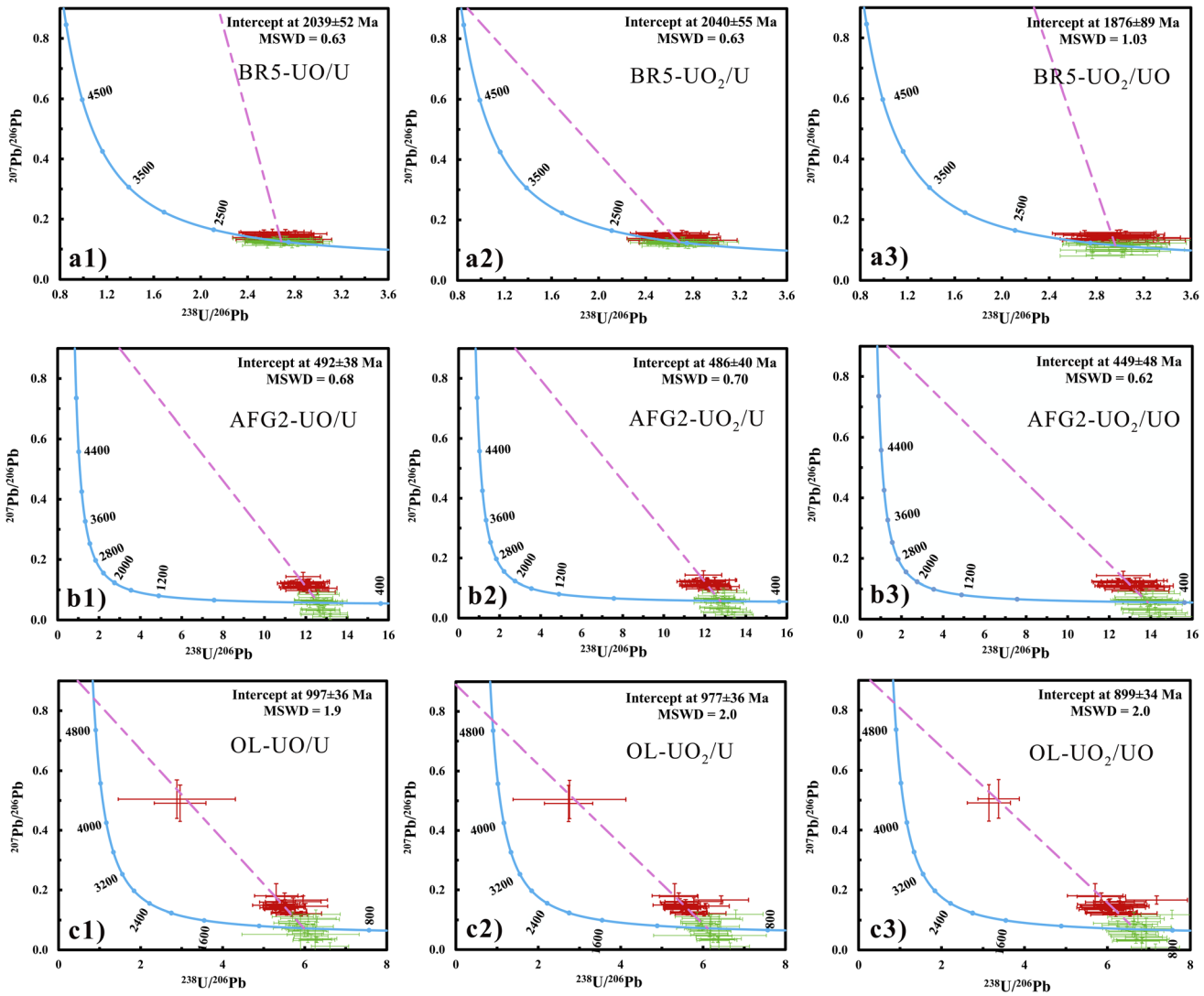

Fig. 5 The 3-D constrained concordia ages of BR5 (a1–a3) AFG2 (b1–b3) and Otter lake (c1–c3) apatites analyzed by the micro primary beam (n = 25, data-point error crosses are 2σ for all results).

Table 2 The diagnostic parameters from the U–Pb results of apatite AFG2

Sample	AFG2	$^{238}U^{+}$	$^{206}Pb^{+}$
Yields (cps ppm^{-1}nA^{-1})	5 nA	1.3	1.6
	500 pA	0.45	0.65

Sample	AFG2	Pb/U *vs.* UO/U	Pb/U *vs.* UO_2/U	Pb/UO *vs.* UO_2/UO
Pb/U error (1σ) (%)	5 nA	1.9	1.9	1.8
	500 pA	3.7	3.9	5.1
Error of intercept age (2σ %)	5 nA	5.0	5.0	4.9
	500 pA	7.7	8.2	10.7
Bias of intercept age (%)	5 nA	0.5	0.3	−1.2
	500 pA	2.8	1.5	−6.2

In order to evaluate the two micro-beam methods, we conducted a comparative analysis of Pb*/U uncertainties in AFG2 apatite using identical calibration protocols between our study and reference data. For clarity, the Pb*/U error of all analysis spots are plotted in Fig. 6 The results demonstrate distinct uncertainty ranges for each method: (1) the 5 nA method yields Pb*/U uncertainties of 1.5–2.5%; (2) the 500 pA method 2 produces Pb*/U uncertainties of 3.5–5.5%. Notably, while reference data show comparable Pb*/U uncertainties (1.5–4.3%), these were obtained using substantially larger beam sizes (>25 μm).[26] Our findings reveal that method 1 achieves comparable precision to the reference methods despite utilizing a 50% reduction in beam size. method 2, while exhibiting slightly higher uncertainties, maintains acceptable precision levels while operating at significantly reduced spatial scales.[26] These results collectively demonstrate that both of our micro-beam methods are viable for *in situ* apatite U–Pb dating, offering distinct advantages in terms of spatial resolution.

Published on 15 August 2025. Downloaded by NANJING UNIVERSITY on 1/21/2026 8:15:39 AM.

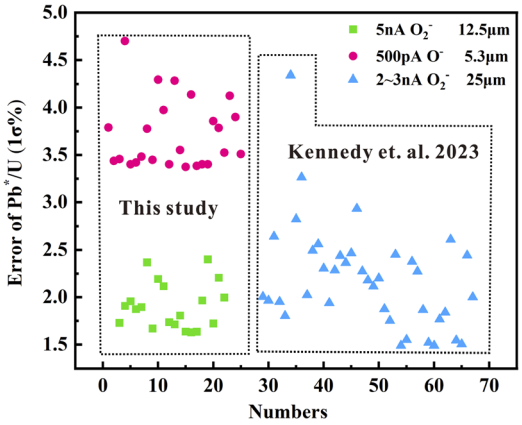

Fig. 6 The error distributions of Pb*/U ratios of AFG2 apatite after calibrating by the BR5 apatite with Pb/U *vs.* UO/U protocol in this study and references.

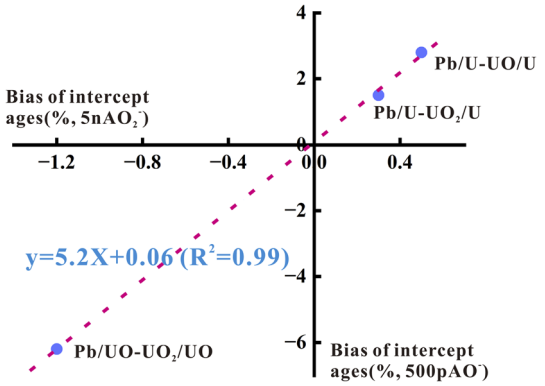

Fig. 7 The relativity of the bias of intercept ages for two methods corresponding to the three calibration protocols (Pb/U *vs.* UO/U, Pb/U *vs.* UO_2/U, Pb/UO *vs.* UO_2/UO).

5.2 Evaluation of calibration protocols for the two analytical methods

Deducing the true $^{206}Pb/^{238}U$ ratios from the highly fractionated measured ratio is an essential procedure during *in situ* SIMS U–Pb analysis. Previous studies have indicated that the relationships between Pb/U *vs.* UO_2 (UO)/U, and Pb/UO *vs.* UO_2/UO can be applied to the calibration of inter-elemental fractionation for many minerals (*e.g.* zircon, apatite, titanite *etc.*).[30,33,43] However, the different calibration protocols may lead to differing age results and errors. Regarding to zircon, it is commonly recommended to use the Pb/UO *vs.* UO_2/UO power law relationship for fractionation calibration and it is the most robust and accurate.[29,44] In this study, we evaluated the above three calibration relationships during *in situ* SIMS apatite U–Pb analysis.

5.2.1 5 nA method. For the data obtained using a 5 nA O_2^- primary beam, we compared the errors of Pb*/U ratios derived from the three power law relationships. As summarized in Table 2, there is no significant difference among errors associated with the Pb/U *vs.* UO/U (1.9%), Pb/U *vs.* UO_2/U (1.9%) and Pb/UO *vs.* UO_2/UO (1.8%) relationships. The precision and accuracy of the dating results were assessed through comprehensive comparison of: (1) error estimates of concordia intercept ages; and (2) systematic biases relative to reference values. While the intercept age errors are consistent across all three relationships, the Pb/UO *vs.* UO_2/UO protocol has a larger systematic bias (−1.2%) compared to the Pb/U *vs.* UO/U (0.5%) and Pb/U *vs.* UO_2/U (0.3%) protocols. The intercept ages of 481 ± 24 Ma, 480 ± 24 Ma and 473 ± 23 Ma, as illustrated in Fig. 4b1–b3, are all consistent with the ID-TIMS age of 478.71 ± 0.22 Ma within the uncertainties.[26] These results demonstrate that each of the three power law relationships can calibrate the inter-elemental fractionation of Pb*/U ratio for the apatite with this primary beam current.

5.2.2 500 pA method. Compared to the results of 5 nA method, the differences between the calibration protocols were particularly pronounced when employing a 500 pA O^- primary beam for analysis. The intercept age bias obtained through the Pb/UO *vs.* UO_2/UO protocol (−6.2%) is four times larger than the bias (1.5%) derived from the Pb/U *vs.* UO_2/U calibration relationship. As shown in Fig. 5b1–b3, the age of 449 ± 23 Ma, derived from the Pb/UO *vs.* UO_2/UO relationship, significantly deviates from the reference age (478.71 ± 0.22 Ma, ID-TIMS). Additionally, the intercept age bias (2.8%) from the Pb/U *vs.* UO/U protocol is larger than that (1.5%) from the Pb/U *vs.* UO_2/U protocol.

For the same method, the AFG2 U–Pb results yield an accurate Pb–Pb age. Hence, the bias in the intercept ages is attributed to the calibration relationships, as the $^{206}Pb^+/^{238}U^+$ ratios remain consistent across the protocols. Fig. 7 displays the relative biases of the intercept ages for both methods. The choice of calibration protocol influences the bias of the intercept ages. Consequently, we recommend using the Pb/U *vs.* UO_2/U calibration protocol to correct for inter-element fractionation when employing a 500 pA micro-beam. In contrast, the Pb/UO *vs.* UO_2/UO relationship is not suitable for apatite U–Pb dating calibration under the same conditions. This conclusion corroborates previous studies employing larger beam sizes,[19] confirming the protocol-dependent nature of fractionation correction accuracy for a low-current of primary beam.

6. Conclusions

This study introduced two LG-SIMS *in situ* micro-apatite U–Pb dating methods: one with high-current (5 nA O_2^-) primary beam and one with a micro-focused (500 pA O^-) primary beam. The micro-focused 500 pA O^- beam generated conical ablation craters (5.3 × 5.3 × 1.4 μm) with minimal sample consumption (~0.03 ng), rendering it particularly advantageous for rare lunar samples. Conversely, the 5 nA O_2^- beam produced larger ablation features (surface: 12.5 × 12.5 μm; depth: 4.1 μm) with ~0.53 ng consumption of apatite, that offers enhanced precision for apatite grains >15 μm. We compared three fractionation calibration protocols (Pb/U *vs.* UO/U, Pb/U *vs.* UO_2/U, and Pb/UO *vs.* UO_2/UO) using the U–Pb ages of AFG2 apatite. Significant systematic biases in U–Pb ages resulted from the Pb/UO *vs.* UO_2/UO calibration protocol (−1.2% for 5 nA O_2^-; −6.1% for 500 pA O^-), exceeding those observed with alternative

 This journal is © The Royal Society of Chemistry 2025

Published on 15 August 2025. Downloaded by NANJING UNIVERSITY on 1/21/2026 8:15:39 AM.

protocols. Consequently, we identify the Pb/UO *vs.* UO_2/UO relationship as unsuitable for apatite fractionation correction. For high-current (5 nA O_2^-) analyses, both Pb/U *vs.* UO/U and Pb/U *vs.* UO_2/U protocols demonstrate comparable efficacy. Of the micro-beam (500 pA O^-) protocols, the Pb/U *vs.* UO_2/U power law calibration is the better choice.

Author contributions

Yue Guan: conceptualization, methodology, investigation and writing-original draft. Jun-Yong Li: conceptualization, writing-review and editing. Allen K. Kennedy: resources, review and editing. De Hong Du: review. Wen-Li Xie: investigation. Lan-Lan Tian: investigation. Xiao-Lei Wang: resources, supervision, funding acquisition, writing-review and editing.

Conflicts of interest

There are no conflicts of interest to declare.

Data availability

The data supporting this article have been included as part of the SI. See DOI: **https://doi.org/10.1039/d5ja00266d**.

Acknowledgements

This work was supported by National Natural Science Foundation of China (42430310, 42241121) and Open Research Fund (2025-Z01) of State Key Laboratory of Critical Earth Material Cycling and Mineral Deposits. The manuscript benefits from the constructive and helpful comments from Yu Liu and another anonymous reviewer. We appreciate Qing Yang and Ze-Xian Cui for providing the Otter lake Apatite and Yan-Qiang Zhang and Ya-Nan Yang for helping with the mount preparation.

References

1 T. Zafar, H. U. Rehman, M. A. Mahar, M. Alam, A. Oyebamiji, S. U. Rehman and C. B. Leng, *J. Geodyn.*, 2020, **136**, 101723.
2 J. Gillespie, A. A. Nemchin, P. D. Kinny, L. Martin, M. Aleshin, M. P. Roberts, T. R. Ireland, M. J. Whitehouse, H. Jeon, A. J. Cavosie and C. L. Kirkland, *Chem. Geol.*, 2021, **559**, 119979.
3 J. Hammerli, N. D. Greber, L. Martin, A. S. Bouvier, A. I. S. Kemp, M. L. Fiorentini, J. E. Spangenberg, Y. Ueno and U. Schaltegger, *Chem. Geol.*, 2021, **579**, 120242.
4 W. Li, F. Costa, C. Oppenheimer and K. Nagashima, *Contrib. Mineral. Petrol.*, 2023, **178**(2), 1–24.
5 E. Bruand, M. Fowler, C. Storey and J. Darling, *Am. Mineral.*, 2017, **102**, 75–84.
6 M. Koike, Y. Sano, N. Takahata, T. Iizuka, H. Ono and T. Mikouchi, *Earth Planet. Sci. Lett.*, 2020, **549**, 116497.
7 C. R. M. McFarlane and J. G. Spray, *Geochim. Cosmochim. Acta*, 2022, **326**, 166–179.
8 L. E. Borg and R. W. Carlson, *Annu. Rev. Earth Planet. Sci.*, 2023, **51**, 25–52.
9 C. R. Walton, H. Jeon, A. Černok, A. S. P. Rae, I. Baziotis, F. Tang, V. S. C. Kuppili, L. Ferrière, J. Darling, S. Hu, M. J. Whitehouse, M. Anand and O. Shorttle, *Geochim. Cosmochim. Acta*, 2023, **359**, 191–204.
10 A. J. Miles, C. M. Graham, C. J. Hawkesworth, M. R. Gillespie and R. W. Hinton, *Mineral. Petrol.*, 2013, **166**, 1–19.
11 Y. Shi, W. Peng, K. H. Joy, X. Yu, Y. Guan, Z. Bao, X. Che, R. Tartèse, J. F. Snape, J. W. Head, M. J. Whitehouse, X. Wang, Y. Qian, Z. Li, C. Wang, T. Long, S. Xie, R. Fan, J. Liu, Z. Yang, C. Yang, P. Wang, S. Liu, Z. Wang, H. Huang, Y. Kang, H. Sun, W. Zhang, L. Tian, H. Li, X. Mao, W. Shan, D. Li, D. Liu and A. A. Nemchin, *Meteorit. Planet. Sci.*, 2024, **59**, 2296–2320.
12 X. Che, A. Nemchin, D. Liu, T. Long, C. Wang, M. D. Norman, K. H. Joy, R. Tartese, J. Head, B. Jolliff, J. F. Snape, C. R. Neal, M. J. Whitehouse, C. Crow, G. Benedix, F. Jourdan, Z. Yang, C. Yang, J. Liu, S. Xie, Z. Bao, R. Fan, D. Li, Z. Li and S. G. Webb, *Science*, 2021, **374**, 887–890.
13 X. Che, T. Long, A. Nemchin, S. Xie, L. Qiao, Z. Li, Y. Ban, R. Fan, C. Yang and D. Liu, *Science*, 2025, **387**, 1306–1310.
14 Z. Cui, Q. Yang, Y. Q. Zhang, C. Wang, H. Xian, Z. Chen, Z. Xiao, Y. Qian, J. W. Head, C. R. Neal, L. Xiao, F. Luo, J. Chen, P. He, Y. Cao, Q. Zhou, F. Huang, L. Chen, B. Wei, J. Wang, Y. N. Yang, S. Li, Y. Yang, X. Lin, J. Zhu, L. Zhang and Y. G. Xu, *Science*, 2024, **386**, 1395–1399.
15 Q. L. Li, Q. Zhou, Y. Liu, Z. Xiao, Y. Lin, J. H. Li, H. X. Ma, G. Q. Tang, S. Guo, X. Tang, J. Y. Yuan, J. Li, F. Y. Wu, Z. Ouyang, C. Li and X. H. Li, *Nature*, 2021, **600**, 54–58.
16 C. Li, H. Hu, M. F. Yang, Z. Y. Pei, Q. Zhou, X. Ren, B. Liu, D. Liu, X. Zeng, G. Zhang, H. Zhang, J. Liu, Q. Wang, X. Deng, C. Xiao, Y. Yao, D. Xue, W. Zuo, Y. Su, W. Wen and Z. Ouyang, *Natl. Sci. Rev.*, 2022, **9**, nwab188.
17 C. Li, H. Hu, M. F. Yang, J. Liu, Q. Zhou, X. Ren, B. Liu, D. Liu, X. Zeng, W. Zuo, G. Zhang, H. Zhang, S. Yang, Q. Wang, X. Deng, X. Gao, Y. Su, W. Wen and Z. Ouyang, *Natl. Sci. Rev.*, 2024, **11**, nwae328.
18 Q. W. L. Zhang, M. H. Yang, Q. L. Li, Y. Liu, Z. Y. Yue, Q. Zhou, L. Y. Chen, H. X. Ma, S. H. Yang, X. Tang, G. L. Zhang, X. Ren and X. H. Li, *Nature*, 2025, **643**, 356–360.
19 Q. L. Li, X. H. Li, F. Y. Wu, Q. Z. Yin, H. M. Ye, Y. Liu, G. Q. Tang and C. L. Zhang, *Gondwana Res.*, 2012, **21**, 745–756.
20 R. A. Stern, S. Bodorkos, S. L. Kamo, A. H. Hickman and F. Corfu, *Geostand. Geoanalytical Res.*, 2009, **33**, 145–168.
21 Y. Liu, Q. L. Li, G. Q. Tang, X. H. Li and Q. Z. Yin, *J. Anal. At. Spectrom.*, 2015, **30**, 979–985.
22 U. Schaltegger, A. K. Schmitt and M. S. A. Horstwood, *Chem. Geol.*, 2015, **402**, 89–110.
23 M. L. Grange, A. A. Nemchin, R. T. Pidgeon, N. Timms, J. R. Muhling and A. K. Kennedy, *Geochim. Cosmochim. Acta*, 2009, **73**, 3093–3107.
24 M. D. Norman and A. A. Nemchin, *Earth Planet. Sci. Lett.*, 2014, **388**, 387–398.

Published on 15 August 2025. Downloaded by NANJING UNIVERSITY on 1/21/2026 8:15:39 AM.

25 J. F. Snape, A. A. Nemchin, M. L. Grange, J. J. Bellucci, F. Thiessen and M. J. Whitehouse, *Geochim. Cosmochim. Acta*, 2016, **174**, 13–29.
26 A. K. Kennedy, J. Wotzlaw, J. L. Crowley, M. Schmitz, U. Schaltegger, B. Wade, L. Martin, C. Talavera, B. Ware and T. H. Bui, *Geostand. Geoanalytical Res.*, 2023, **47**, 373–402.
27 D. M. Chew, P. J. Sylvester and M. N. Tubrett, *Chem. Geol.*, 2011, **280**, 200–216.
28 Y. Sano, T. Oyama, K. Terada and H. Hidaka, *Chem. Geol.*, 1999, **153**, 249–258.
29 H. Jeon and M. J. Whitehouse, *Geostand. Geoanalytical Res.*, 2015, **39**, 443–452.
30 Q. L. Li, X. H. Li, Y. Liu, G. Q. Tang, J. H. Yang and W. G. Zhu, *J. Anal. At. Spectrom.*, 2010, **25**, 1107–1113.
31 Y. Liu, X. H. Li, Q. L. Li, G. Q. Tang and Q. Z. Yin, *J. Anal. At. Spectrom.*, 2011, **26**, 845–851.
32 W. Yang, Y. T. Lin, J. C. Zhang, J. L. Hao, W. J. Shen and S. Hu, *J. Anal. At. Spectrom.*, 2012, **27**, 479–487.
33 Q. L. Li, X. H. Li, Y. Liu, F. Y. Wu, J. H. Yang and R. H. Mitchell, *Chem. Geol.*, 2010, **269**, 396–405.
34 T. R. Ireland and I. S. Williams, *Rev. Mineral. Geochem.*, 2003, **53**, 215–241.
35 R. H. Steiger and E. Jäger, *Earth Planet. Sci. Lett.*, 1977, **36**, 359–362.
36 K. R. Ludwig, *User's Manual for Isoplot Version 3.75–4.15: a Geochronological Toolkit for Microsoft Excel*, Berkeley Geochronological Center Special Publication, Berkeley, 2012.
37 I. Wendt, *Chem. Geol.*, 1984, **46**, 1–12.
38 K. Terada, Y. Sasaki, M. Anand, Y. Sano, L. A. Taylor and K. Horie, *Earth Planet. Sci. Lett.*, 2008, **270**, 119–124.
39 C. H. Chung, C. F. You, J. W. Schopf, N. Takahata and Y. Sano, *Precambrian Res.*, 2020, **349**, 105564.
40 M. C. Liu, K. D. McKeegan, T. M. Harrison, G. Jarzebinski and L. Vltava, *Int. J. Mass Spectrom.*, 2018, **424**, 1–9.
41 P. Ptáček, *Apatites and Their Synthetic Analogues-Synthesis, Structure, Properties and Applications*, InTechOpen, London, 2016.
42 J. L. Hao, W. Yang, S. Hu, R. Li, J. L. Ji, H. G. Changela and Y. T. Lin, *J. Anal. At. Spectrom.*, 2021, **36**, 1625–1633.
43 A. K. Schmitt and T. Zack, *Chem. Geol.*, 2012, **332–333**, 65–73.
44 N. Takahata, Y. Tsutsumi and Y. Sano, *Gondwana Res.*, 2008, **14**, 587–596.
45 J. S. Stacey and J. D. Kramers, *Earth Planet. Sci. Lett.*, 1975, **26**, 207–221.

 This journal is © The Royal Society of Chemistry 2025